Astronomical Techniques and Instruments, Vol. 1, March 2024, 128–139

Article Open Access

Solar image reconstruction method under atmospheric turbulence at Fuxian Lake Solar Observatory

Sizhong Zou[1,3], Zhenyu Jin[1,2], Kaifan Ji[1,2], Jun Xu[1,2], Lei Yang[1,2*]

[1]*Yunnan Observatories*, *Chinese Academy of Sciences*, *Kunming* 650216, *China*

[2]*Yunnan Key Laboratory of Solar Physics and Space Science*, *Kunming* 650216, *China*

[3]*University of Chinese Academy of Sciences*, *Beijing* 101408, *China*

*Correspondence: yanglei@ynao.ac.cn

Received: November 30, 2023; Accepted: December 26, 2023; Published Online: March 6, 2024; https://doi.org/10.61977/ati2024010

Citation: Zou, S. Z., Jin, Z. Y., Ji, K. F., et al. 2024. Solar image reconstruction method under atmospheric turbulence at Fuxian Lake Solar Observatory. *Astronomical Techniques and Instruments*, **1**(2): 128−139. https://doi.org/10.61977/ati2024010.

Abstract: Strong atmospheric turbulence reduces astronomical seeing, causing speckle images acquired by ground-based solar telescopes to become blurred and distorted. Severe distortion in speckle images impedes image phase deviation in the speckle masking reconstruction method, leading to the appearance of spurious imaging artifacts. Relying only on linear image degradation principles to reconstruct solar images is insufficient. To solve this problem, we propose the multiframe blind deconvolution combined with non-rigid alignment (MFBD-CNRA) method for solar image reconstruction. We consider image distortion caused by atmospheric turbulence and use non-rigid alignment to correct pixel-level distortion, thereby achieving nonlinear constraints to complement image intensity changes. After creating the corrected speckle image, we use the linear method to solve the wavefront phase, obtaining the target image. We verify the effectiveness of our method results, compared with others, using solar observation data from the 1 m new vacuum solar telescope (NVST). This new method successfully reconstructs high-resolution images of solar observations with a Fried parameter r_0 of approximately 10 cm, and enhances images at high frequency. When r_0 is approximately 5 cm, the new method is even more effective. It reconstructs the edges of solar graining and sunspots, and is greatly enhanced at mid and high frequency compared with other methods. Comparisons confirm the effectiveness of this method, with respect to both nonlinear and linear constraints in solar image reconstruction. This provides a suitable solution for image reconstruction in ground-based solar observations under strong atmospheric turbulence.

Keywords: Astronomical seeing; Solar telescopes; Solar observatories; Astronomy image processing; Phase error; Deconvolution

1. INTRODUCTION

Atmospheric turbulence has always been the main factor limiting the resolution of ground-based solar telescope imaging systems, causing acquired images to be fuzzy, distorted and randomly displaced. To describe atmospheric turbulence with respect to optics, Fried postulated that the physical definition of seeing is the coherence diameter of the turbulent atmosphere, expressed by parameter r_0 in cm. The better the seeing, the higher the r_0 value. The Fried parameter can be expressed as

$$r_0 = 0.185\cos^{\frac{3}{5}}(\gamma)\left[\frac{\lambda^2}{\int_0^H C_N^2(h)\,\mathrm{d}h}\right]^{\frac{3}{5}}, \quad (1)$$

where γ is the zenith angle of the observed object, λ is the wavelength of the observing band, h is the height above ground, $C_N^2(h)$ is the refractive index structure constant of the atmosphere and H is the total height of the turbulent atmosphere[1].

Liu et al. and Lou et al. have conducted long-term on-site atmospheric visualization tests at the Fuxian Lake Solar Observatory (FLSO)[2,3]. Table 1 lists the annual mean seeing data at FLSO monitored by the solar difference image motion monitor from 1999 to 2002. In Table 1, r_0 is uncalibrated; r_0* is calibrated to the zenith and can be categorized into boundary layer seeing r_0B and free atmosphere seeing r_0F. From these data, the distribution of seeing at FLSO is not ideal. FLSO has more sunny days in winter and spring than in summer and fall, but the monthly mean seeing is generally lower than annual

Table 1. Statistical information of the monthly average atmospheric seeing at Fuxian Lake Solar Observatory from 1999 to 2002. Values are in cm. r_0: the monthly average atmospheric seeing. r_0*: the monthly average atmospheric seeing calibrated to the zenith. r_0B: the monthly average boundary layer seeing. r_0F: the monthly average free atmosphere seeing [1]

	May.	Jun.	Jul.	Aug.	Sept.	Oct.	Nov.	Dec.	Jan.	Feb.	Mar.	Apr.
r_0	10.42	12.91	14.29	13.44	11.07	9.34	9.26	7.84	6.85	6.74	7.67	8.42
r_0*	10.82	14.52	15.03	14.46	12.63	11.25	12.07	10.40	9.62	7.76	9.05	9.32
r_0B	13.70	18.25	17.16	15.60	13.06	11.35	12.30	10.73	9.74	8.25	11.39	12.13
r_0F	21.18	28.94	39.71	52.03	73.16	139.09	98.56	62.27	98.14	31.21	18.00	17.33

mean seeing. When strong turbulence occurs in the free atmosphere, r_0 reduces to 4−6 cm, causing short-exposure images acquired by ground-based solar telescopes to suffer from severe distortion and degradation.

Presently, the NVST uses the speckle masking method to reconstruct high-resolution solar images[4,5]. Representative of statistical reconstruction methods, speckle interferometry[6] and speckle masking[7] have become mainstream solar image reconstruction methods. Speckle masking reconstructs the modes and phases of target images based on the statistical properties of short-exposure speckle images of each order. The statistical method used in speckle masking to describe the influence of atmospheric turbulence on images is of physical significance.

Because the speckle masking method is based on the triply correlated speckle images, the phase of the target image is estimated recursively from the low-frequency phase to the high-frequency phase. The recursive process will inevitably be affected by noise, such as photon noise, which accumulates in the high-frequency component, potentially causing noticeable distortion of the fine structure of the object.

Consequently, in the winter and spring when free atmospheric turbulence activity is strong, the resolution of FLSO images reconstructed by speckle masking will be significantly reduced. Full image quality cannot be accurately restored, and imaging artifacts will appear. This can be verified through image data from January to April in each year at the website, http://fso.ynao.ac.cn.

Another class of solar image reconstruction techniques uses the inverse convolution method, which mainly includes the blind deconvolution method and phase diversity. Blind deconvolution refers to the technique of estimating the target image directly from a small number of short-exposure images without prior knowledge of the point spread function (PSF). The multiframe blind deconvolution (MFBD) algorithm[8] estimates the target image based on the principle of maximum likelihood, by employing a sequence of short-exposure solar speckle images. The phase diversity technique is a further refinement of blind deconvolution, introducing a known aberration (e.g. defocus) into the imaging system in addition to the target focal plane image[9,10]. Then, images are obtained, and the uncertainty of the phase recovery is eliminated by using two (or more) images. Löfdahl & Scharmer unified the problems of phase diversity and MFBD into the problem of solving the wavefront phase coefficients under the linear constraints of maximum likelihood theory, and the phase diversity method can be regarded as a special MFBD technology with stronger constraints[11].

The flaws of the inverse convolution method are also obvious. It relies only on the degraded image as an input value, and uses an optimization algorithm to find the wavefront phase and target image close to the real solution. The deconvolution method ignores the existence of severe aberration and random displacements when r_0 decreases. Therefore, it cannot accurately describe the nonlinear influence of atmospheric turbulence on short-exposure images, and the accuracy of the restored wavefront phase is also greatly reduced.

In recent years, Liu et al. proposed Non-rigid Alignment-based Solar Image Reconstruction (NASIR), which is an image reconstruction method suitable for fast searching and filtering data[12]. This method uses the novel application of a computational optical flow image method to obtain image phase information by using pixel-by-pixel non-rigid alignment of each group image based on a reference frame. Non-rigid alignment is the correction between pixels according to a small area in the image, which is different to the overall size image displacement of the speckle images. NASIR can reconstruct the whole field at once without splitting the image into sub-blocks, substantially reducing the required reconstruction time. However, this method only considers nonlinear correction of aligned image aberration, and ignores the use of linear constraints to reconstruct the phase from further image information.

This paper proposes the MFBD-CNRA solar image reconstruction technique. This algorithm yields improved image alignment and phase recovery. Primary considerations are as follows. (1) Effects of distortion and random displacement on short-exposure images, caused by strong atmospheric turbulence. We rationalize the geometrical form and structure of a sequence of speckle images using the non-rigid alignment technique, and the accurate alignment of images between frames is realized. (2) In poor seeing conditions, short-exposure images contain broken structures. It is necessary to use an improved frame selection method to select lucky images with sufficient high-frequency information and stable structure to restrict the general structural shape of the target, preventing the image from reconstructing the wrong deviation structure. (3) Using the non-rigid aligned average frame to supplement the a priori knowledge of the target image, we obtain the initial values of wavefront Zernike aberration coefficients in the optimization process. Searching from reliable ini-

tial values effectively limits the confidence interval of optimization and avoids falling into local optima prematurely. (4) Anisotropic filters are used to effectively smooth and suppress noise, and restore image details.

Here, we present the specific principles and methods in Section 2. Section 3 presents observational NVST data and experimental results. Section 4 discusses the advantages and disadvantages of MFBD-CNRA and the role of non-rigid alignment. Finally, we summarize the results of our work and future plans.

2. TECHNIQUES AND METHODS

The MFBD-CNRA image reconstruction technique is still essentially a wavefront phase estimation and target recovery method based on image intensity. However, the process of image reconstruction considers the nonlinear degradation process of the solar speckle pattern, which compensates for the lack of linearity.

To correct the distortion and displacement of speckle images caused by atmospheric turbulence, the non-rigid alignment technology uses the principle of optical flow (explained in Section 2.1) to align each frame of short-exposure images with the reference image (RI) pixel by pixel, completing the inter-frame image alignment and yielding the corrected short-exposure image sequence. On this basis, image sub-blocks are segmented, and the lucky frame selection strategy (explained in Section 2.2) based on spectral ratio and structural similarity are adopted to select the images with more high-frequency information and stable structure as input images for MFBD. The averaged frame image of the post-alignment speckle image sub-blocks is taken as the prior target image. The initial value of the phase iteration of the cost generalization function is derived to effectively narrow the confidence interval of the optimization search. An anisotropic filter is introduced to smooth and suppress noise while restoring the image. Finally, the recovered image is stitched to reconstruct the large field-of-view image.

The above principle involves key steps such as non-rigid alignment technique, lucky frame selection method, estimation of wavefront phase Zernike coefficients, and denoising.

2.1. Non-rigid Alignment Technique

For ground-based solar telescopes, the short-exposure image has the problems of distortion and random displacement caused by atmospheric turbulence. The traditional way to solve this problem is to shift the whole image using the inter-correlation method, but this rigid alignment (i.e., with the same amount of displacement of pixels at different positions in the image) only overcomes the displacement problem, and cannot eliminate the aberration of different regions in the short-exposure image.

In computational vision processing, the optical flow method is often used to establish the relationship model between the image intensity change and displacement field for target detection in moving images, to obtain the displacement of each pixel of the target between consecutive image frames, and finally to get the motion trajectory of the spatial target. Non-rigid alignment draws on the principle of the optical flow method to establish the relationship model between pixel displacement and intensity change for solar speckle images. However, unlike calculating the motion consistency of adjacent frames in the field of visual processing, the adjacent frame in the field of solar astronomy has random displacement and distortion. Consequently, it is impossible to accurately calculate the displacement field of short-exposure sequence images by relying on the adjacent frame images.

When MFBD-CNRA adopts the optical flow method, it is necessary to select an appropriate reference frame. For each frame of the sequence of speckle images, the optical flow vector between the reference image and the speckle image is calculated to recover the different displacements on each image area.

This pixel-by-pixel "non-rigid" displacement is different from the overall rigid movement of the whole image, and it can reasonably and efficiently correct the target's aberration displacement in the spatial domain. At the same time, major alignment between the frames is accomplished based on the same reference image.

2.1.1. *Selection of the initial reference image*

Accurate estimation of the displacement field needs an image with a high signal-to-noise ratio as a reference frame. When constructing a reference frame for the first time, the phase of the average frame image is obtained by superimposing short-exposure sequence images filtered by the band-pass filter, and the mode is obtained according to the statistical reconstruction of speckle interferometry. After combining the mode and the phase, a reference frame image with a stable structure and high-frequency information is obtained.

The initial reference frame image mode is reconstructed as

$$|RI(u)|^2 = \left\langle |I(u)|^2 \cdot \frac{Otf(u)}{Sitf(u) + S_{\text{noise}}} \right\rangle , \tag{2}$$

where u is the frequency domain coordinates, $I(u)$ is the speckle image, S_{noise} is the estimated noise power spectrum in the speckle images, $Otf(u)$ is the ground-based solar telescope theoretical optical transfer function, which is related to the shape of the telescope pupil and the aperture, and $Sitf(u)$ is the theoretical speckle interferometry transfer function, which is estimated by the seeing[13]. The angle brackets denote taking the average value.

2.1.2. *Calculate the displacement field*

The pixel intensity distribution in the localized region of the solar speckle image can be expressed as

$$f(\boldsymbol{x}) \approx \boldsymbol{x}^{\mathrm{T}} \boldsymbol{A} \boldsymbol{x} + \boldsymbol{b}^{\mathrm{T}} \boldsymbol{x} + c, \tag{3}$$

where x is the two-dimensional coordinates of the speckle image region, $f(\boldsymbol{x})$ is the image pixel intensity at the location, $\boldsymbol{A}$ is a symmetric matrix variable, $\boldsymbol{b}$ is a vector, and c is a scalar.

We assume that the approximate expression for the pixel intensity distribution of the reference frame is

$$f_1(\boldsymbol{x}) \approx \boldsymbol{x}^{\mathrm{T}}\boldsymbol{A}_1\boldsymbol{x} + \boldsymbol{b}_1^{\mathrm{T}}\boldsymbol{x} + c_1, \tag{4}$$

when the speckle image has an ideal translation transformation with this region of the reference image, the expression for the relationship between pixel intensity and position in this region of the speckle image and the reference frame image is as follows:

$$\begin{aligned} f_2(\boldsymbol{x}) &= f_1(\boldsymbol{x}-\boldsymbol{d}) = (\boldsymbol{x}-\boldsymbol{d})^{\mathrm{T}}\boldsymbol{A}_1(\boldsymbol{x}-\boldsymbol{d}) + \boldsymbol{b}_1^{\mathrm{T}}(\boldsymbol{x}-\boldsymbol{d}) + c_1 \\ &= \boldsymbol{x}^{\mathrm{T}}\boldsymbol{A}_1\boldsymbol{x} + (\boldsymbol{b}_1 - 2\boldsymbol{A}_1\boldsymbol{d})^{\mathrm{T}}\boldsymbol{x} + \boldsymbol{d}^{\mathrm{T}}\boldsymbol{A}_1\boldsymbol{d} - \boldsymbol{b}_1^{\mathrm{T}}\boldsymbol{d} + c_1 \\ &= \boldsymbol{x}^{\mathrm{T}}\boldsymbol{A}_2\boldsymbol{x} + \boldsymbol{b}_2^{\mathrm{T}}\boldsymbol{x} + c_2. \end{aligned} \tag{5}$$

When the displacement d satisfies Eq. (5), the coefficients are equal and it follows that

$$\begin{aligned} \boldsymbol{A}_2 &= \boldsymbol{A}_1 \\ \boldsymbol{b}_2 &= \boldsymbol{b}_1 - 2\boldsymbol{A}_1\boldsymbol{d} \\ c_2 &= \boldsymbol{d}^{\mathrm{T}}\boldsymbol{A}_1\boldsymbol{d} - \boldsymbol{b}_1^{\mathrm{T}}\boldsymbol{d} + c_1, \end{aligned} \tag{6}$$

which leads to the relation

$$\boldsymbol{d} = -\frac{1}{2}\boldsymbol{A}_1^{-1}(\boldsymbol{b}_2 - \boldsymbol{b}_1). \tag{7}$$

Therefore, we can develop a calculation model for the image pixel intensities of translation transformations. When we assume that the displacement field is only slowly varying so that the information can be integrated within the neighborhood of each pixel, we try to find the amount of translation d in Equation (7) in the neighborhood of the image region, given by

$$\boldsymbol{d} = \left(\sum_n w_n \boldsymbol{A}_n^{\mathrm{T}}\boldsymbol{A}_n\right)^{-1} \sum_n \left(w_n \boldsymbol{A}_n^{\mathrm{T}}\Delta\boldsymbol{b}_n\right), \tag{8}$$

where n is a pixel point within the neighborhood, w_n is a way of calculating the weight of the pixel points in the neighborhood, and $\Delta\boldsymbol{b}_n$ is the difference between $\boldsymbol{b}_n$ and the reference frame vector $\boldsymbol{b}$.

To describe the projection of the distortion on the image more accurately, a more reasonable calculation model of the displacement field can be obtained through optimization strategies such as the affine transformation of the displacement field and the weighting of neighborhood pixels[12]. For the projection of general 3D motion on the image plane, the displacement field is represented by a 2D 8-parameter model as

$$\boldsymbol{d}_x(x,y) = a_1 + a_2x + a_3y + a_7x^2 + a_8xy, \tag{9}$$

$$\boldsymbol{d}_y(x,y) = a_4 + a_5x + a_6y + a_7xy + a_8y^2, \tag{10}$$

which can be written as a matrix,

$$\boldsymbol{d} = \boldsymbol{S}\boldsymbol{P}, \tag{11}$$

$$\boldsymbol{S} = \begin{pmatrix} 1 & x & y & 0 & 0 & 0 & x^2 & xy \\ 0 & 0 & 0 & 1 & x & y & xy & y^2 \end{pmatrix}, \tag{12}$$

$$\boldsymbol{P} = \begin{pmatrix} a_1 & a_2 & a_3 & a_4 & a_5 & a_6 & a_7 & a_8 \end{pmatrix}^{\mathrm{T}}. \tag{13}$$

So, we get

$$\boldsymbol{P} = \left(\sum_n w_n \boldsymbol{S}_n^{\mathrm{T}}\boldsymbol{A}_n^{\mathrm{T}}\boldsymbol{A}_n\boldsymbol{S}_n\right)^{-1} \sum_n \left(w_n \boldsymbol{S}_n^{\mathrm{T}}\boldsymbol{A}_n^{\mathrm{T}}\Delta\boldsymbol{b}_n\right). \tag{14}$$

When the displacement field is slowly changing, the unknown quantity $\boldsymbol{A}_n$ and $\Delta\boldsymbol{b}_n$ of all pixel points in the neighborhood are the same. The least squares method is used to solve the equation $\boldsymbol{P}$ relating the intensity of multiple pixels in the neighborhood to the translation vector. Then, according to Equation (11), the translation vector $\boldsymbol{d}$ of the pixel points of the speckle images in the local region, with respect to the pixel points of the reference image, can be derived. This is extended to the whole image area, and the displacement field is established between the speckle images and the reference image.

2.1.3. *Reference image update with iterative alignment*

After the initial reference frame is set, each pixel in the set area of each speckle image frame finds the corresponding pixel in the reference frame, and obtains the displacement field corresponding to the two pixels. Then, the distortion displacement of the speckle image can be recovered pixel by pixel by inverse displacement and interpolation, according to the solved displacement field vector. Performing a single non-rigid alignment of all speckle images in the sequence is referred to as a "round". The reference frame of each subsequent round is set to be the average frame of the speckle image sequence after the completion of the previous round, to continuously improve the signal-to-noise ratio of the reference image, which is conducive to a more accurate restoration of distortion. After the preset number of correction rounds is reached, the distortion displacement field of each frame is calculated, and every original short-exposure image is moved pixel by pixel according to the finally calculated displacement field for complete alignment with the reference frame, correcting the geometry and structure of the image sequences.

2.2. Lucky Frame Selection Method

Each group of collected solar data contains 200 speckle images. During the observation process, there are likely to be errors in some images due to telescope pointing errors and weather conditions. It is wise to select images that are less affected by atmospheric turbulence, which will retain more high-frequency information and be closer to the true target image.

The lucky frame selection technology[14] used by NVST is a frame selection method based on speckle interferometry. The less the image is affected by atmospheric turbulence, the larger the value of its transfer function will be in each frequency band. We divide the power spectrum of the single-frame short-exposure image by the average of the speckle image power spectrum to normalize and obtain $\varepsilon(u, v)$ which is related to the telescope and the atmosphere. $O(u, v)$ is the frequency domain representation of the target image, and $H(u, v)$ is the frequency domain representation of the PSF.

$$\epsilon(u,v)=\frac{|I(u,v)|^2}{\langle|I(u,v)|^2\rangle}=\frac{|O(u,v)|^2}{\langle|O(u,v)|^2\rangle}\frac{|H(u,v)|^2}{\langle|H(u,v)|^2\rangle}=\frac{|H(u,v)|^2}{\langle|H(u,v)|^2\rangle} \tag{15}$$

We can evaluate image quality using circular integration. Here, δ represents the integral of $\varepsilon(u, v)$ in the frequency domain, expressed as

$$\delta=\int_0^{2\pi}\mathrm{d}\theta\int_{\rho_1(r_0)}^{\rho_2(r_0)}\rho\varepsilon(\rho\cos\theta,\ \rho\sin\theta)\,\mathrm{d}\rho, \tag{16}$$

where ρ represents the frequency magnitude of the radial, $\rho_1(r_0)$ and $\rho_2(r_0)$ represent the integral ring inner diameter outer diameter, and r_0 is the average seeing of the image.

However, this method does not consider the problem of image structure fragmentation and distortion caused by rapidly moving atmospheric turbulence. Consequently, it is not sensitive to image structure stability, and performs poorly at rejecting images containing broken and distorted structures. After the non-rigid geometric correction, it is necessary to select the lucky images with more high-frequency information and stable structure to constrain the overall structure of the target to prevent the deviation of image reconstruction in the process of MFBD. Structural similarity (SSIM)[15] is a measure of the similarity between two images. Given a single image and the mean frame image, it is given by

$$SSIM(X,Y)=\frac{(2\mu_x\mu_y+c_1)(2\sigma_{xy}+c_2)}{(\mu_x^2+\mu_y^2+c_1)(\sigma_x^2+\sigma_y^2+c_2)}, \tag{17}$$

where μ_x is the mean of X; μ_y is the mean of Y; σ_x is the variance of X; σ_y is the variance of Y; and σ_{xy} is the covariance between X and Y; $c_1 = (k_1L)$, $c_2 = (k_2L)$ are constants used to maintain stability, L is the range level of pixel values, $k_1 = 0.03$, $k_2 = 0.03$; and the range of $SSIM$ is −1 to 1. When the two images are identical, $SSIM$ is equal to 1. The frame selection evaluation criterion used in this paper is given by

$$LuckIndex=\delta\cdot SSIM\,. \tag{18}$$

2.3. Estimation of Wavefront Phase Zernike Coefficients

The short-exposure image can be viewed as a multiplication of the target image and the PSF of the system in the frequency domain. For the convenience of formula expression and to avoid misunderstanding, in the following formula, the two-dimensional coordinates (u, v) of the image are expressed as a single coordinate (u), given by

$$I(u)=O(u)\cdot H(u)\,. \tag{19}$$

MFBD can recover the target and estimate the instantaneous PSF or wavefront phase information of the system by establishing the error cost function and finding the minimum values for the aberration coefficient and target estimation. To determine the degree of approximation between the intensity of the reconstructed target image and the intensity of the actual acquired speckle image, we can define an error cost generalization function based on the principle of maximum likelihood estimation, expressed as

$$E(O,a_m)=\sum_j^J\left|I_j\left(u\right)-O(u)\cdot H_j(u)\right|^2, \tag{20}$$

where a_m denotes the wavefront phase Zernike coefficient corresponding to the mth term, and j denotes the jth frame of the speckle image in a set of input images.

Löfdahl adds Tikhonov regular terms about the target and phase to the error cost function, and the function is expressed as[16]

$$E(O,a)=\sum_j^J\left|I_j\left(u\right)-O(u)\cdot H_j(u)\right|^2+\gamma|O(u)|^2+\alpha J(\phi), \tag{21}$$

$$J(\phi)=\frac{1}{2}\sum_m^M\frac{1}{\lambda_m}\sum_j^J|a_{jm}|^2, \tag{22}$$

where γ is the Tikhonov regular term parameter for target estimation, α is the Tikhonov regular term parameter for wavefront phase information estimation, and λ_m is the covariance matrix corresponding to the mth term of the orthogonal polynomials.

Therefore, the problem of how to estimate the wavefront information and the target image from the multi-frame speckle image can be transformed into a problem of solving the cost generalized function with respect to the minimal values of the variable O and the phase information a, when the target image and the system PSF are unknown. We can apply linear optimization to the cost generalized function, but it is inefficient to solve two unknowns directly and the calculation easily converges prematurely.

In this paper, we take an approach that complements the prior knowledge of the target image. Consequently, we choose to use the non-rigid corrected mean short-exposure image O_n as the initial priori estimate of the target.

This leads to the solution, the expression is

$$E(O_n,a)=\sum_j^J\left|I_j\left(u\right)-O(u)\cdot H_j(u)\right|^2+\gamma|O_n(u)|^2+\alpha J(\phi),\tag{23}$$

after replacing the target estimate O with O_n, solving for the first-order partial derivative of the cost generalized function $E(O,\ a)$ with respect to the unknown quantity a, and thus solving for a set of aberration coefficients $a_{\mathrm{m-initial}}$, such that $E(O_n,\ a)$ is minimized under the condition that the initial image O_n is known.

Considering the reduction of the number of unknowns to eliminate the objective image O, Löfdahl simplifies $E(O,\ a)$ as[16]

$$E(a)=\left[\sum_j^J|I_j|^2-\frac{\left|\sum_j^J I_j^*\cdot H_j\right|^2}{\sum_j^J|H_j|^2+\gamma}\right]+\frac{\alpha}{2}\sum_m^M\frac{1}{\lambda_m}\sum_j^J|a_{jm}|^2.\tag{24}$$

The initial iteration value of $a_{\mathrm{m-initial}}$ is used as the initial iteration value of the $E(a)$ optimization solving process. Equation (24) is solved iteratively from the initial value, and the iteration is stopped when the maximum number of iterations is reached or the resultant value meets the set error value. Eventually, the final resultant value of aberration coefficients a_m is calculated.

By setting the initial iteration value, the search interval of the final solution is greatly constrained, and some local optimal values are skipped, thereby converging to more accurate aberration coefficients. By using the phase aberration coefficients and Zernike's formula, we reconstruct the PSF of the telescope.

2.4. Construction of the Image Filter

In actual observation, speckle images usually have additional noise. The key to estimating the clear image from the blurred image is to make an appropriate strategy between obtaining the clear target image and restraining the noise. The solar short-exposure image with additional noise can be expressed as

$$I(u)=O(u)\cdot H(u)+Noise(u)\ .\tag{25}$$

Due to the existence of noise and the influence of the PSF in suppressing high-frequency information, the signal-to-noise ratio of the image is insufficient, and the direct deconvolution method will lead to serious noise and ringing in the target image.

Wiener filtering is a linear filtering method based on the minimum mean square error criterion[17], but the power spectra of the noisy and clear images are difficult to obtain accurately in practical problems. An approximate ratio is commonly used to estimate in specific applications, which still leaves a lot of noise in images with low signal-to-noise ratios. The Tikhonov regularization denoising method[17], in the form of frequency domain truncation, can suppress the amplification of noise energy caused by the energy decay of the PSF at high frequencies. When the regularization parameter is not selected properly, it will produce a serious ringing effect, causing unclear edges in the recovered image.

To better deal with noise and image details, we construct a filter in the form[11]

$$Filter=1-\left\langle\sum_j^J Noise_j\right\rangle\left\langle\frac{\sum_j^J|H_j|^2}{|\sum_j^J I_j\cdot H_j^*|^2}\right\rangle,\tag{26}$$

where $Noise_j$ is the estimated noise power spectrum outside the selected cutoff frequency, and the angle brackets represent taking the mean average value. We then set the values of *Filter* to 0.2−1, and all values less than 0.2 and greater than 1 to 0. All isolated peaks in the filter that cannot be connected to the zero-frequency peak are removed to obtain a smooth filter. This constructs a filter that satisfies anisotropy by calculating the ratio of the noise to the signal at different locations, effectively smoothing and suppressing the noise.

3. RESULTS

The main scientific goal of NVST is to carry out high-resolution imaging and spectral observation of the sun in the 0.3−2.5 micron band, including measuring the fine structure and evolution process of the solar magnetic field with high temporal and spatial resolution. The telescope has a vacuum sealing window with a diameter of 1 200 mm, an effective telescope aperture of 980 mm, an effective field of view of more than 3', and a focal length of 45 m at F_3.

At present, the channels of the high-resolution imaging system are mainly the chromosphere H-alpha (center wavelength 656.26 nm, channel bandwidth 0.025 nm), and the photosphere TiO (center wavelength 705.8 nm, channel bandwidth 1 nm). The TiO channel is a common optical channel for observing the solar photosphere, and the reconstruction of TiO data is representative of solar observations in all bands.

The experimental data in Table 2 are all Level 0 observations in the TiO band from 2020 to 2022. Each batch consists of 200 short-exposure images, each with an exposure time of approximately 0.15 s. The atmospheric Fried parameters r_0 of the experimental data are calculated by the spectral ratio method[18].

3.1. With Seeing of Approximately 1.5"

In summer and autumn, the seeing at FLSO is usually approximately 1.5" and the Fried parameter r_0 is above 10 cm. The speckle masking reconstruction effect is quite good. Fig. 1 and Fig. 2 show the reconstruction results of data sets 1 and 2 using speckle masking, MFBD, NASIR, and MFBD-CNRA.

As can be seen, the result images of all algorithms clearly show details such as sunspot, solar graining and

Table 2. Solar speckle image reconstruction test data set from the NVST. Information includes experimental data number, observation band, observation time, observation area, r_0

Data No.	Band	Time	Area	r_0 /cm
1	TiO	2021-09-30 UT 05:38:42	12880	11.70
2	TiO	2020-12-08 UT 03:57:16	12790	10.06
3	TiO	2020-10-06 UT 01:27:41	12882	9.31
4	TiO	2021-11-29 UT 04:02:58	12898	7.35
5	TiO	2023-03-06 UT 06:31:57	13242	5.32
6	TiO	2023-01-20 UT 03:50:04	12297	4.90

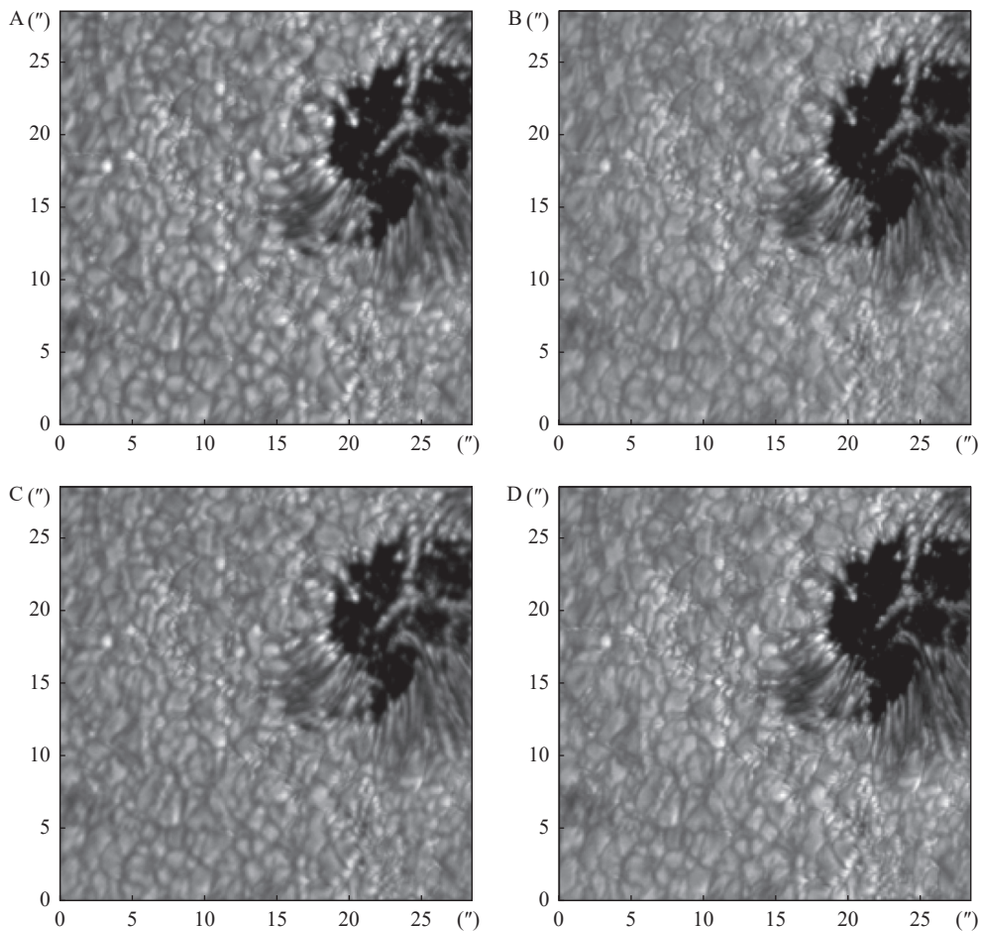

Fig. 1. Reconstruction results of NVST TiO 2021-09-30 UT 05:38:42, observation active area 12880, from (A) Speckle masking, (B) MFBD, (C) NASIR, (D) MFBD-CNRA.

solar magnetic highlights. Visually, the four algorithms are close in reconstruction quality. To intuitively compare the quality in the frequency domain, we convert the 2D power spectrum image to polar coordinates, then average along the polar angle to obtain a 1D power spectrum curve with the length of the polar diameter as the frequency and the average intensity as the energy. In Fig. 3, we plot the power spectrum curves of the reconstructed image of Fig. 2. The power spectrum curve of MFBD-CNRA image is higher than the other curves in the mid and high frequency region, which is closer to the limiting resolution of the telescope. Fig. 4 shows the intensity profile at the red line pixels and supports the correctness of the MFBD-CNRA intensity distribution.

To describe the quality of image reconstruction more accurately, indicators such as SSIM and the coefficient of variation of the intensity profile (CVoIP) are used to analyze each result. The SSIM index can be used to evaluate differences between images by combining three different factors: brightness, contrast and structure. CVoIP, which is the ratio of the standard deviation of the intensity profile to its mean, can measure the difference in image contrast.

The results of quantitative comparison between speckle masking and the other three methods are given in Table 3, which shows that the reconstructed images of speckle masking have high correlation and SSIM with those of NASIR and MFBD-CNRA. The quantitative analysis indices show that the reconstructed images of

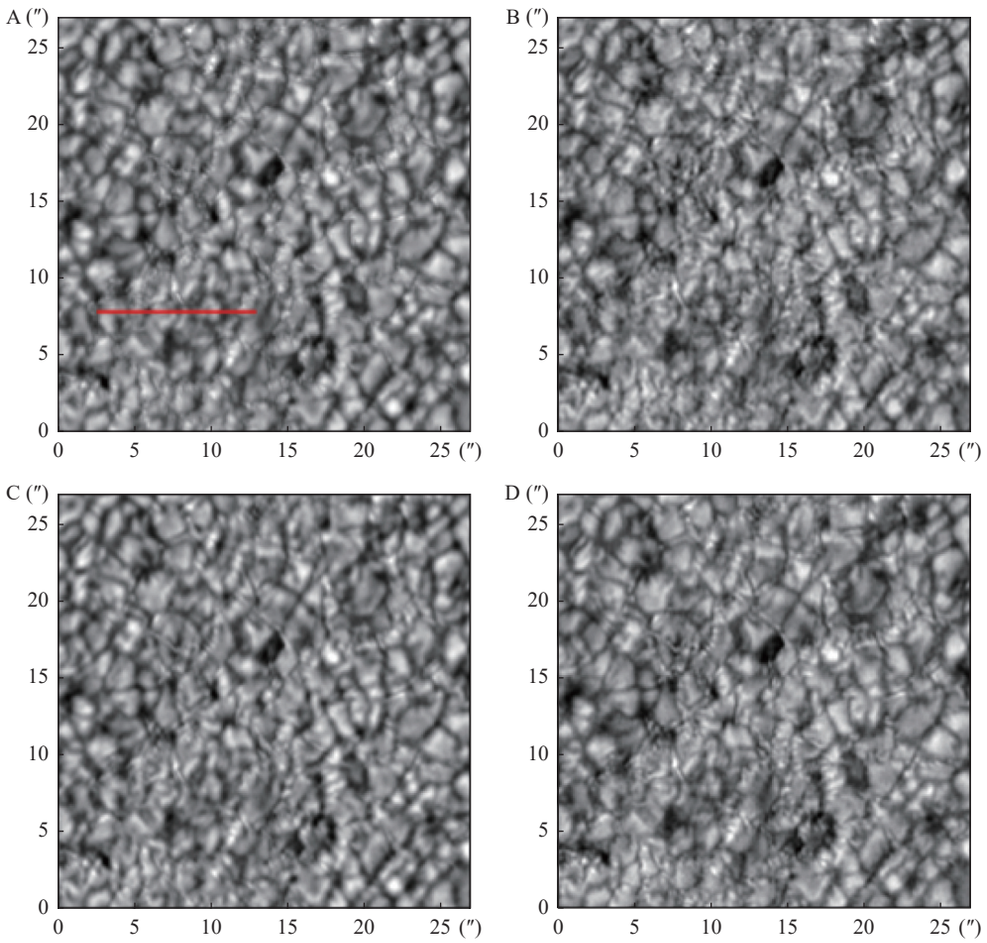

Fig. 2. Reconstruction results of NVST TiO 2020-12-08 UT 03:57:16, observation active area 12790, from (A) Speckle masking, (B) MFBD, (C) NASIR, (D) MFBD-CNRA.

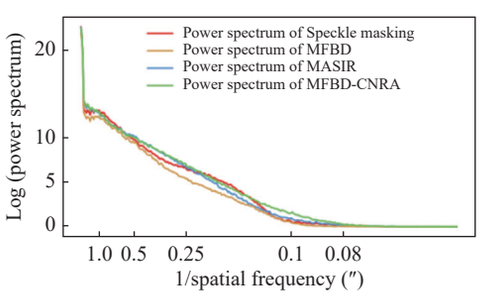

Fig. 3. Power spectrum curves of reconstruction results of NVST TiO 2020-12-08 UT 03:57:16, observation active area 12790.

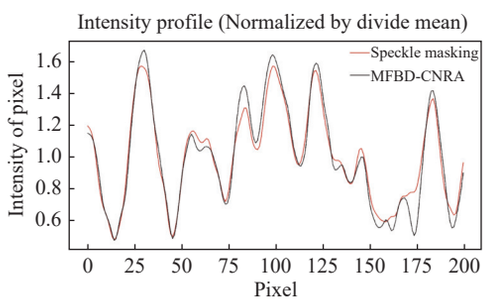

Fig. 4. Comparison of the intensity profiles between the reconstruction results (the red line region in Fig. 2 A) of speckle masking and MBFD-CNRA.

Table 3. Quantitative comparison of the reconstruction results from four solar image reconstruction algorithms of test data in Table 1

Observation Time	r_0	SSIM				CVoIP			
		Masking	MFBD	NASIR	MFBD-CNRA	Masking	MFBD	NASIR	MFBD-CNRA
2021-09-30 UT 05:38:42	11.70	1	0.971 03	0.975 12	0.975 22	0.317 12	0.309 67	0.314 04	0.317 77
2020-12-08 UT 03:57:16	10.06	1	0.843 35	0.873 72	0.907 97	0.241 95	0.238 16	0.264 22	0.265 48
2020-10-06 UT 01:27:41	9.31	1	0.931 70	0.965 54	0.949 84	0.161 91	0.135 52	0.164 08	0.170 23
2021-11-29 UT 04:02:58	7.35	1	0.786 35	0.830 14	0.848 13	0.273 82	0.238 48	0.272 24	0.258 25
2023-03-06 UT 06:31:57	5.32	0.324 34	0.847 51	0.831 51	1	0.165 79	0.196 04	0.245 11	0.256 33
2023-01-20 UT 03:50:04	4.90	0.524 34	0.883 35	0.907 97	1	0.201 95	0.226 14	0.245 22	0.273 64

NASIR and MFBD-CNRA are close to speckle masking when seeing is good, and even exceed speckle masking in image contrast.

3.2. With Seeing of Approximately 3 Arcseconds

In FLSO short-exposure image data, the seeing reaches the lowest from January to March every year, usually approximately 3". And r_0 range is usually 4 cm to 5 cm. As seeing declines, the high-frequency information of the speckle image is severely impaired after atmospheric effects, and the signal-to-noise ratio also begins to decrease. Fig. 5 illustrates the reconstruction results for data set 5. Fig. 6 shows reconstruction results of data set 6 for comparison. These two sets of data are representative of low seeing data in actual observation. With the weakening of seeing, the phase recursion error gradually accumulates, and the reconstruction results of the speckle-mask method show spurious structures, which have a great impact on the reconstructed images. The multi-frame blind deconvolution algorithm can reconstruct solar graining in the local area, but detailed structures such as sunspot contours, penumbral filaments, and edges of the solar graining cannot be revealed.

The NASIR algorithm image does not contain spurious structures and shows low-frequency information such as the contours of the solar graining. However, in the NASIR algorithm, there is an error in the reconstruction for the penumbra portion: The penumbra portion has no real contrast. The high-frequency structures of the MFBD-CNRA algorithm are better than the results of the other reconstruction algorithms, retaining a realistic contrast.

In Fig. 7, we draw the power spectrum outline of the reconstructed image of data set 5. The MFBD power spectral profile decreases significantly, and the speckle masking power spectral profile also decreases rapidly in the high-frequency region. The power spectrum curves for the NASIR and MFBD-CNRA images are very close in the mid and high frequency regions, and they are both higher than the other methods. Fig. 8 shows the intensity curve of the red line in Fig. 5, showing that the quality of the reconstructed image using MFBD-CNRA gradually improves.

4. DISCUSSION

The reconstruction of observational data by comparing MFBD and MFBD-CNRA verify the necessity of non-rigid alignment, which is a nonlinear constraint, to solve the problem of solar image degradation. Meanwhile,

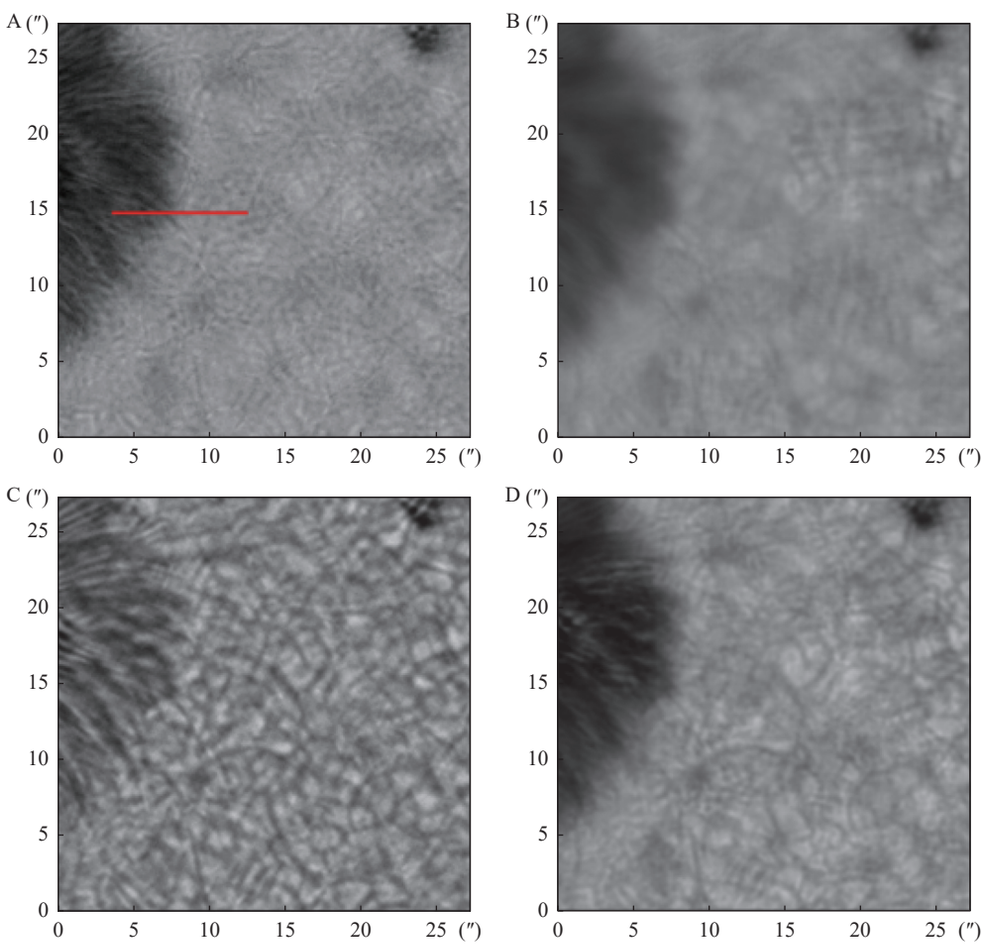

Fig. 5. Reconstruction results of NVST TiO 2023-03-06 UT 06:31:57 at observation active area 13242, from (A) Speckle masking, (B) MFBD, (C) NASIR, (D) MFBD-CNRA.

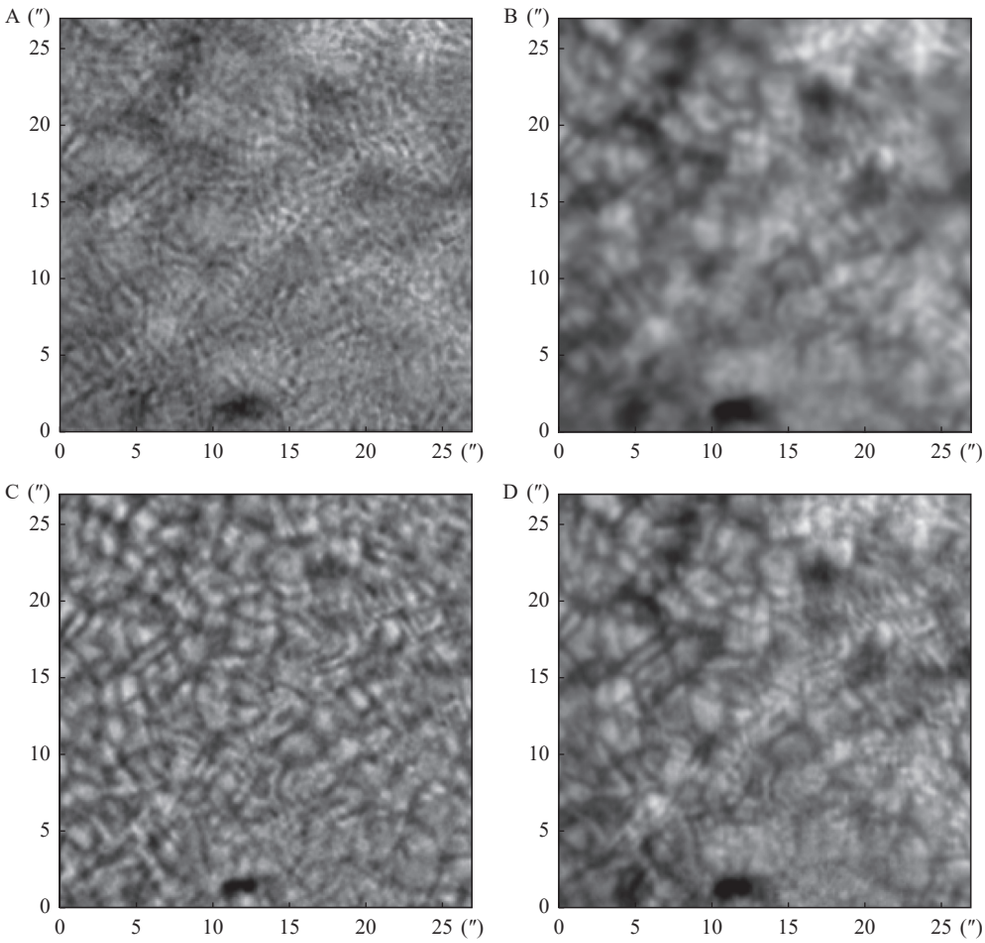

Fig. 6. Reconstruction results of NVST TiO 2023-01-20 UT 03:50:04, observation active area 12297, from (A) Speckle masking, (B) MFBD, (C) NASIR, (D) MFBD-CNRA.

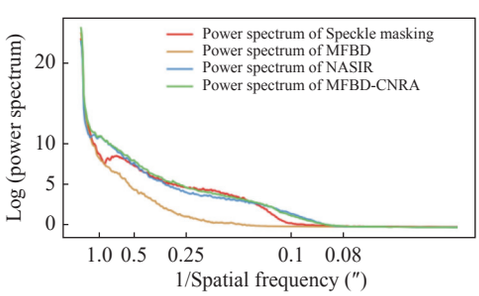

Fig. 7. Power spectrum curves of reconstruction results of NVST TiO 2023-03-06 UT 06:31:57, observation active area 13242.

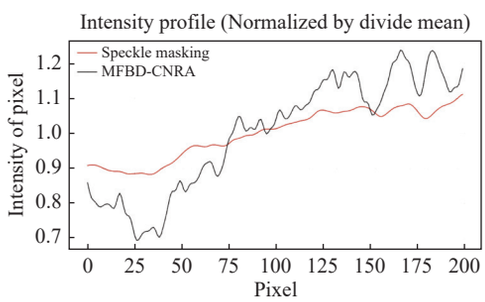

Fig. 8. Comparison of the intensity profile between the reconstruction results (the red line region in Fig. 5A) of speckle masking and MBFD-CNRA.

comparing the results of NASIR and MFBD-CNRA, we find that the high-resolution images cannot be reconstructed perfectly without optimizing the solving phase by linear constraint either.

4.1. The Role of Non-rigid Alignment

To solve the problem of solar image reconstruction, we must consider the effect of the atmosphere on the image. Fig. 9 shows the average frames of the initial speckle frame sequence and the average frames of the sequence from the first through fifth alignments. Fig. 10 illustrates the power spectrum curves of Fig. 9A and F.

Geometrically, non-rigid alignment eliminates the influence of random image displacement caused by atmospheric turbulence. The pixel alignment between the corrected image sequences is improved, which is more conducive to overcoming strong turbulence.

From the power spectrum curve, the reconstructed image after correction has a good enhancement effect in the mid and high frequency area. This is helpful for the reconstructed image resolution to be closer to the diffraction limit of the telescope.

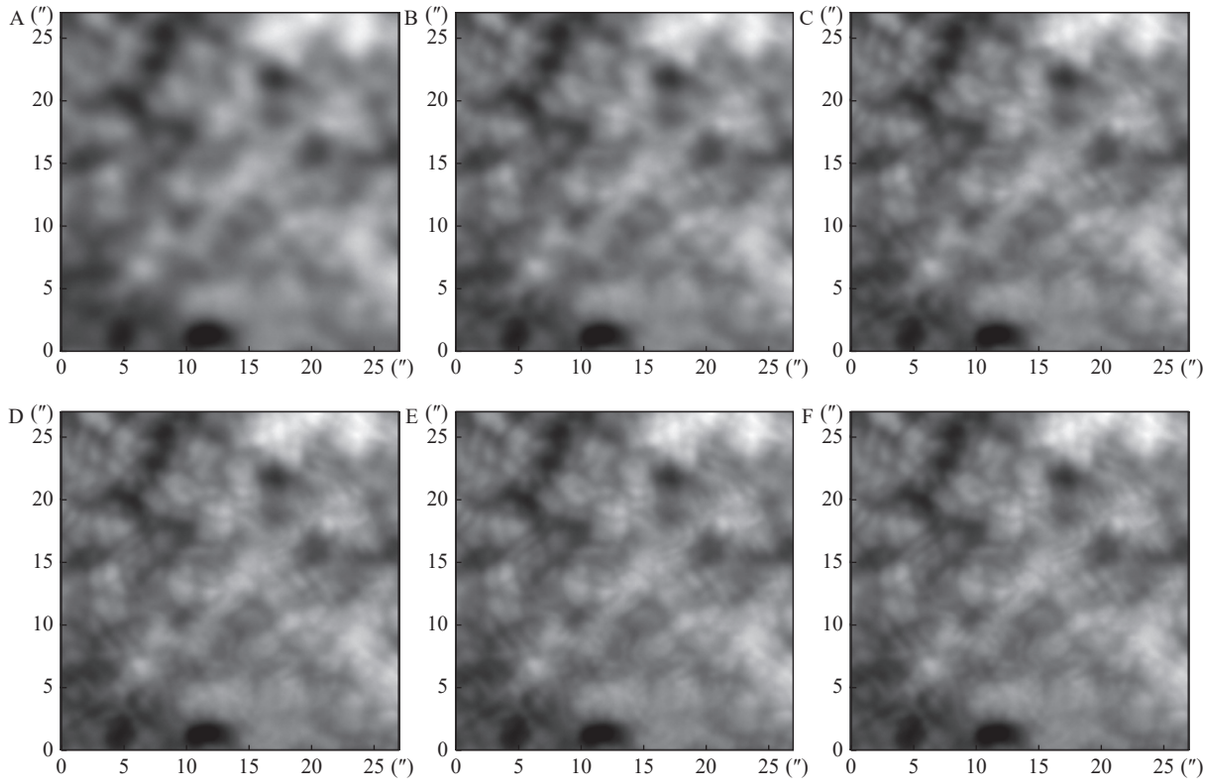

Fig. 9. Average frame images of NVST TiO 2023-01-20 UT 03:50:04, observation active area 12297. (A) The average frame image before alignment. (B) to (F)： The average frame images after 1st to 5th non-rigid alignment.

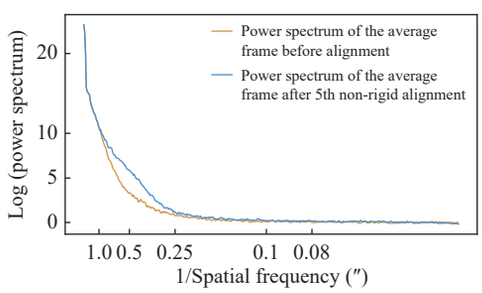

Fig. 10. Comparison of power spectral curves.

4.2. Necessary Linear Constraint

NASIR shows some improvement in the power spectrum but still lacks in the image phase, because it only merges the mean frame phase and the interferometry speckle mode into a rebuilt image. The disadvantage of this method is that the calculated Sitf is the same for each value of r_0 without considering the variability of the actual image. MFBD-CNRA solves the phase close to the true value through the linear constraint method. For different groups of input images, it is possible to compute the corresponding PSF. Depending on the corrected image and the calculated PSF, the reconstructed image can be solved more satisfactorily.

4.3. Further Improvements of MFBD-CNRA

While achieving successful experiments, MFBD-CNRA deserves further optimization and improvement in the following areas:

(1) Number of iterations. Non-rigid alignment based on speckle imaging requires a reference image. It should be noted that the number of iterations for the reference image here is roughly five, and it is not the case that more corrections are more effective. The next step of the optimization strategy should be to build a reasonable model and choose the number of frame iterations according to the value of r_0.

(2) Time efficiency. The MFBD-CNRA reconstruction time efficiency is slower than NASIR and does not improve significantly over the time efficiency of the speckle masking method. The reason is that it still needs to perform the processes of sub-block splitting, reconstruction, and stitching together the final image. Further work is needed to optimize the algorithm for high-performance parallel computing to improve the reconstruction efficiency.

(3) Phase optimization. Phase reconstruction is a difficult problem, and this work currently still reconstructs the phase by employing the same solution method used to solve the Zernike coefficients. Traditional linear optimization methods are effective but may not be ideal. Utilizing deep learning to search for phase coefficients is also a promising method to consider in future work.

5. CONCLUSION

Strong atmospheric turbulence in winter and spring leads to a significant decrease in the seeing at FLSO, and the reconstruction of solar images using the masking and

MFBD methods is poor. Combining the advantages of the non-rigid alignment method and phase reconstruction, we propose a new solar image reconstruction method, termed the MFBD-CNRA method, which successfully obtains high-resolution images under strong turbulence. The reconstructed image results from NVST observational data show the robustness and applicability of the MFBD-CNRA algorithm in cases where the r_0 parameter is less than 6 cm.

Non-rigid alignment is a nonlinear method that can overcome atmospheric turbulence's effect. The main effect is pixel-by-pixel alignment of images and correction of aberrations, thereby allowing the target image to retain more high-frequency information. Considering the differences in actual images, linear constraints are essential in the accurate calculation of PSF.

For day-to-day solar telescope observations, MFBD-CNRA can effectively process data, allowing continuous data collection in the event of sudden unfavorable changes in weather conditions. The MFBD-CNRA algorithm can compensate for algorithm-level defects in data reconstruction in the case of strong atmospheric turbulence.

Future work will involve parallelization of the MFBD-CNRA algorithm to further improve reconstruction efficiency. This study can provide an effective reference for data reconstruction pipelines in other ground-based solar telescopes.

ACKNOWLEDGMENTS

This work is sponsored by the National Natural Science Foundation of China (NSFC) under the grant numbers (11773073, 11873027, U2031140, 11833010), Yunnan Key Laboratory of Solar Physics and Space Science under the number 202205AG070009, Yunnan Provincial Science and Technology Department (202103AD50013, 202105AB160001, 202305AH340002), the GHfund A202302013242 and CAS "Light of West China" Program 202305AS350029.

AUTHOR CONTRIBUTIONS

Sizhong Zou and Lei Yang conceived the ideas, Sizhong Zou implemented the study and wrote the paper. Lei Yang and Jun Xu collected the data, Zhenyu Jin and Kaifan Ji improved the algorithm and innovation. All authors read and approved the final manuscript.

DECLARATION OF INTERESTS

Zhenyu Jin is an associate editor-in-chief number and Kaifan Ji is an editorial board member for Astronomical Techniques and Instruments. They are not involved in the editorial review or the decision to publish this article. The authors declare no competing interests.

REFERENCES

[1] Chen, L. H., Liu, Z., Chen, D. 2019. Climatological analysis of the seeing at Fuxian Solar Observatory. *Research in Astronomy and Astrophysics*, **19**(1): 015.

[2] Liu, Z., Lou, K., Zhang, R. L., et al. 2000. The day-time seeing monitor at Fuxian lake and some primary results. *Publication of Yunnan Observatory*, **4**(4): 95−100. (in Chinese)

[3] Lou, K., Liu, Z., Zhang, R. L., et al. 2001. The site testing day of daytime seeing and vapor from Fuxian lake. *Progress In Astronomy*, **19**(2): 147−150. (in Chinese)

[4] Xiang, Y. Y., Liu, Z., Jin, Z.Y., et al. 2016. High resolution solar image reconstruction. *Progress In Astronomy*, **34**(1): 94−110. (in Chinese)

[5] Xiang, Y. Y., Liu, Z., Jin, Z.Y. 2016. High resolution reconstruction of solar prominence images observed by the New Vacuum Solar Telescope. *New Astronomy*, **49**: 8−12.

[6] Xiang, Y. Y., Jin, Z. Y. 2011. Simulation and analysis of signal-to-noise ratios for statistics of speckle interferometry. *Astronomical Research and Technology*, **8**(3): 293−297, 305. (in Chinese)

[7] Liu, Z., Xu, J., Gu, B. Z.,et al. 2014. New vacuum solar telescope and observations with high resolution. *Research in Astronomy and Astrophysics*, **14**(6): 705−718.

[8] Van Noort, M.,Van Der Voort, L. R., Löfdahl, M. G. 2005. Solar image restoration by use of multi-frame blind deconvolution with multiple objects and phase diversity. *Solar physics*, **228**(1/2): 191−215.

[9] Yu, X. G., Liu, Z., Jin, Z. Y., et al. 2010. Design of a phase diversity wavefront sensor. *Astronomical Research and Technology*, **7**(1): 55−59. (in Chinese)

[10] Yang L., Liu, Z., Jin, Z. Y., et al. 2009. The effect of uncertainty in defocus distanceon the wave-front reconstruction with the phase diversity algorithm. *Astronomical Research and Technology*, **6**(1): 43−50. (in Chinese)

[11] Löfdahl, M. G., Scharmer, G. B. 1994. Wavefront sensing and image restoration from focused and focused solar images. *Astronomy and Astrophysics, Supplement Series*, **107**(2): 243−264.

[12] Liu, H., Jin, Z. Y., Xiang, Y. Y., et al. 2022. High resolution solar image reconstruction based on non-rigid alignment. *Research in Astronomy and Astrophysics*, **22**(9): 095005

[13] Li, M. L., Xiang, Y. Y., Jin, Z. Y., et al. 2018. The analysis of anisoplanatism's influence in different econstruction sub-block size of NVST. *Astronomical Research and Technology*, **15**(1): 87−94. (in Chinese)

[14] Liu, C. Y., Xiang, Y. Y., Jin, Z. Y. 2014. Image processing with frame selection for Hα solar chromosphere images. *Astronomical Research and Technology*, **11**(2): 140−144. (in Chinese)

[15] Wang, Z., Bovik, A. C., Sheikh, H. R., et al. 2004. Image quality assessment: from error visibility to structural similarity. *IEEE Transactions on Image Processing*, **13**(4): 600−612.

[16] Löfdahl, M. G. 2002. Multi-frame blind deconvolution with linear equality constraints. In Society of Photo-Optical Instrumentation Engineers (SPIE) Conference Series. DOI:10.1117/12.451791.

[17] Hang, Y. 2022. Survey of non-blind image restoration. *Chinese Optics*, **15**(5): 954−972. (in Chinese)

[18] Hu, G., Xiang, Y. Y., Liu, Z., et al. 2021. Seeing estimation accuracy study based on a sequence of speckle images. *Astronomical Research and Technology*, **18**(2): 213−225. (in Chinese)